electronics

MDPI

Communication

Synthesis of Non-Mirror-Symmetrical Far-Field Patterns Using Two Parallel Current Sheets

Gaobiao Xiao *, Ting Zang and Rui Liu

State Key Laboratory of Radio Frequency Heterogeneous Integration, Department of Electronic Engineering, Shanghai Jiao Tong University, Shanghai 200240, China
* Correspondence: gaobiaoxiao@sjtu.edu.cn

Abstract: This paper shows that the radiation patterns and polarizations on the two sides of the source plane can be controlled separately if two parallel current sheets are used. An efficient algorithm is proposed to determine the propagation components of the currents on the two sheets directly from the specified radiation pattern. Numerical examples demonstrate that the algorithm is effective for synthesizing radiation patterns with complex footprints and beam-wise polarizations. Although the resultant continuous current distribution is not easy to implement in practical applications, it provides a useful base for further designs. If proper feeding techniques are developed, it will also be possible to spatially sample the continuous current distribution and realize the radiation pattern with large scale antenna arrays.

Keywords: antenna array synthesis; degree of freedom; radiation field

check for updates

Citation: Xiao, G.; Zang, T.; Liu, R. Synthesis of Non-Mirror-Symmetrical Far-Field Patterns Using Two Parallel Current Sheets. *Electronics* **2023**, *12*, 892. https://doi.org/10.3390/electronics12040892

Academic Editor: Paolo Baccarelli

Received: 9 January 2023
Revised: 2 February 2023
Accepted: 7 February 2023
Published: 9 February 2023

Copyright: © 2023 by the authors. Licensee MDPI, Basel, Switzerland. This article is an open access article distributed under the terms and conditions of the Creative Commons Attribution (CC BY) license (https://creativecommons.org/licenses/by/4.0/).

1. Introduction

The synthesis of antenna arrays is a very important task in many applications [1–8]. Up to now, the synthesis methods may be roughly divided into two groups. The first kinds of approaches are based on optimization techniques such as the genetic algorithms (GAs) [9,10], particle swarm optimization (PSO) [11], simulated annealing (SA) [12], sequential convex optimizations [13,14], ant colony optimization method [15], and some other algorithms [16–23]. These optimization methods are powerful and successful in antenna synthesis. However, optimization algorithms are usually time-consuming to achieve optimal solutions. Moreover, the synthesis time increases exponentially with the increase in the number of unknowns. Therefore, it may become quite difficult to use optimization methods for the synthesis of very large antenna arrays.

The second group includes the direct synthesis methods. These methods generally aim to realize patterns of discrete sources or continuous linear sources. As early as 1946, Woodward and Lawson proposed the realization of a desired pattern by sampling it at various discrete locations and interpolating it using a composing function that is associated with a harmonic current of a uniform amplitude distribution and uniform progressive phase [24]. The excitation of the source is then obtained by summing the harmonic currents required for the interpolation. Prony's method [25,26] can be used to realize a specified pattern by determining the strengths of the N point sources at complex positions, z_α and $\alpha = 1, \ldots, N$, and each element has a directivity that can be slightly controlled by the real part of the position. A comprehensive review can be found in [27].

For a linear current or a single layer of the rectangular current sheet, its far field can be directly calculated using the Fourier transformation. Generally, the current can be expanded with harmonic components with the Fourier series, and the field generated by each harmonic component of the current is referred to as mode field [28]. A mode can be regarded as a propagation one if at the direction of the peak of its main radiation lobe, it can propagate away from the source and contribute to the far field. Otherwise, it is an evanescent mode, and it decays at the direction of its peak exponentially when it leaves the

source. The far field can then be approximately expressed with the superposition of the values at the peak direction of those propagation modes using sinc interpolation functions. Consequently, the harmonic components of the current corresponding to these propagation modes can be directly obtained from the far-field values at these sampling directions. If the current sources are spatially band-limited and consist of only propagation harmonic components, i.e., the harmonic components of currents corresponding to the propagation modes, then the relationship between the radiation pattern and the current distribution is rigorous [28]. Unfortunately, a practical current is usually not spatially band-limited. Part of the side lobes corresponding to the evanescent modes may also contribute to the far-field pattern. In this case, the synthesis can only be carried out in an approximate way. However, this method is still of significance, because it can provide a solid base for further improvement.

The method is demonstrated to be effective to determine the propagation harmonic components of the linear source or a single-current sheet, in which the radiation pattern is axially symmetrical with respect to the linear source, or mirror-symmetrical, with respect to the source plane. Obviously, their application range may be limited because of this symmetry. In some situations, we may need to control the radiation pattern on both sides of the source plane. At each side, it may be required to form different beams with different polarizations to cover a different area, as shown in Figure 1. A natural solution is to use two antenna arrays placed back-to-back for this purpose, with one array responsible for one side. In order to avoid interference between the two arrays, we have to carefully design the arrays to reduce the level of their back lobes, or add metal backplanes between them to reduce mutual couplings.

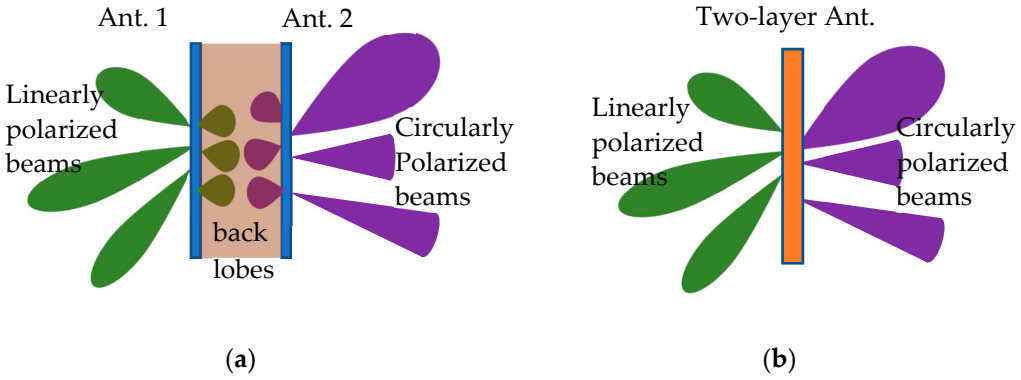


Figure 1. Concept for possible applications of radiators consisting of two current sheets. (**a**) Two separate arrays. (**b**) Single antenna with two current sheets.

As has been shown in [29], if two parallel layers of current sheets are used to replace the single-current sheet, the degree of freedom (DoF) of the far fields can be doubled. However, the DoF will no longer significantly increase if more than two layers of current sheets are added. Therefore, we can use two layers of current sheets to remove the symmetry of far fields and control the radiation pattern in the two sides separately. It is possible to inspire new designs that may be more compact or efficient than using two separate antenna arrays.

This paper will extend the direct synthesis method to the case of two parallel current sheets. Due to the phase difference caused by the displacement of the current sheets, the far-field pattern is generally not mirror-symmetrical anymore. It will be shown that the propagation components of the currents on the two sheets can also be directly synthesized, based on the prescribed far-field pattern in the upper half space and the lower half space. The synthesis procedure is described and demonstrated with numerical examples.

2. Direct Synthesis Algorithm

The far electric field $\mathbf{E}$ at position $\mathbf{r}$ of a current source $\mathbf{J}$ in source region V_s can be generally expressed as the following:

$$\mathbf{E}(\mathbf{r}) = -j\omega\mu\left(\bar{\mathbf{I}} - \hat{\mathbf{a}}_r\hat{\mathbf{a}}_r\right)\cdot\frac{e^{-jkr}}{4\pi r}\int_{V_s} e^{j\mathbf{k}\cdot\mathbf{r}'}\mathbf{J}\left(\mathbf{r}'\right)d\mathbf{r}' \tag{1}$$

where $\mathbf{k} = k_x\hat{\mathbf{a}}_x + k_y\hat{\mathbf{a}}_y + k_z\hat{\mathbf{a}}_z$ is the wave vector, $\hat{\mathbf{a}}_r$ is the radial unit vector, and $\bar{\mathbf{I}}$ is the identity operator. k is the wavenumber and μ is the permeability in free space. For a current source on a rectangular sheet parallel to the xoy plane with a size of $D_x \times D_y$ and with its center locating at $(0, 0, d)$, its far field can be separated into two polarizations,

$$\mathbf{F}(\theta,\varphi) = -\sin\theta_x\hat{\boldsymbol{\theta}}_x\int_{-D_y/2}^{D_y/2}\int_{-D_x/2}^{D_x/2} e^{jk_xx+jk_yy}e^{jk_zd}I_x(x,y)dxdy - \sin\theta_y\hat{\boldsymbol{\theta}}_y\int_{-D_y/2}^{D_y/2}\int_{-D_x/2}^{D_x/2} e^{jk_xx+jk_yy}e^{jk_zd}I_y(x,y)dxdy \tag{2}$$

where θ_x is the angle between the position vector $\mathbf{r}$ and the x-axis, and θ_y is that with the y-axis. $\hat{\boldsymbol{\theta}}_x$ and $\hat{\boldsymbol{\theta}}_y$ are, respectively, the corresponding unit vectors, as shown in Figure 2. Note that (2) includes a phase term, $\exp(jk_zd)$, due to the offset of the current sheet in the z-axis. The primes for the source coordinates are omitted in the expressions as there is no risk of confusing here. In the spherical coordinate system, we have $k_x = k\sin\theta\cos\varphi$, $k_y = k\sin\theta\sin\varphi$, and $k_z = k\cos\theta$.

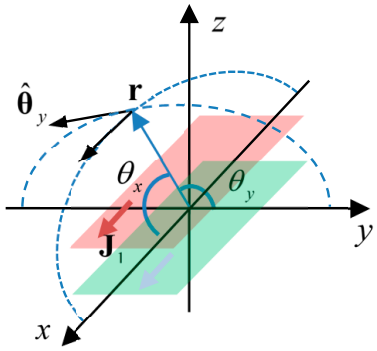


Figure 2. Current sheet and the unit vectors in the coordinate system.

The factor $\sin\theta_x$ and $\sin\theta_y$ in (2) come from the x-polarized infinitesimal dipole and the y-polarized infinitesimal dipole composing the current sheets. Furthermore, (2) reveals that the x-component and the y-component of the current can be handled separately because their far fields are separatable at every direction in the following way:

$$\mathbf{F}(\theta,\varphi)\cdot\hat{\boldsymbol{\theta}}_x = -\sin\theta_x\int_{-D_y/2}^{D_y/2}\int_{-D_x/2}^{D_x/2} e^{jk_xx+jk_yy}e^{jk_zd}I_x(x,y)dxdy \tag{3}$$

$$\mathbf{F}(\theta,\varphi)\cdot\hat{\boldsymbol{\theta}}_y = -\sin\theta_y\int_{-D_y/2}^{D_y/2}\int_{-D_x/2}^{D_x/2} e^{jk_xx+jk_yy}e^{jk_zd}I_y(x,y)dxdy \tag{4}$$

Consider the two current sheets shown in Figure 2. They are placed parallel to the xoy plane. Both sheets are rectangularly shaped with the same size of $D_x \times D_y$, $D_x = N_x\lambda$, and $D_y = N_y\lambda$, where λ is the wavelength and N_x and N_y are the two integers. The center of the upper current $\mathbf{J}_1$ locates at $(0, 0, d)$, while that of the lower current sheet $\mathbf{J}_2$ locates at $(0, 0, -d)$. We consider the 2-D array factor of the x-polarization alone, as the y-polarization

can be independently handled in exactly the same away. The x-polarized radiation pattern of the two current sheets can be expressed as [28],

$$F_{2a}(\theta,\varphi)=\frac{1}{D_xD_y}\int_{-D_y/2}^{D_y/2}\int_{-D_x/2}^{D_x/2}e^{jk_xx+jk_yy}\times\left[e^{jk_zd}I_1(x,y)+e^{-jk_zd}I_2(x,y)\right]dxdy \quad (5)$$

Here, we have added a constant factor $1/(D_xD_y)$. The two layers of the currents are separately expanded with the 2-D Fourier series,

$$\begin{cases} I_1(x,y)=\sum\limits_{m=-\infty}^{\infty}\sum\limits_{n=-\infty}^{\infty}I_{1mn}e^{j(m\Omega_xx+n\Omega_yy)} \\ I_2(x,y)=\sum\limits_{m=-\infty}^{\infty}\sum\limits_{n=-\infty}^{\infty}I_{2mn}e^{j(m\Omega_xx+n\Omega_yy)} \end{cases} \quad (6)$$

where $\Omega_x=2\pi/D_x$ and $\Omega_y=2\pi/D_y$ Substituting (6) into (5) provides the following:

$$F_{2a}(\theta,\varphi)=\sum_{m=-\infty}^{\infty}\sum_{n=-\infty}^{\infty}\left(I_{1mn}e^{jk_zd}+I_{2mn}e^{-jk_zd}\right)f_{mn}(\theta,\varphi) \quad (7)$$

The 2-D mode function $f_{mn}(\theta,\varphi)$ for the x-polarization is the same as that of the single-layer sheet with its center at the origin,

$$f_{mn}(\theta,\varphi)=\mathrm{sinc}\left[\frac{D_x}{2}(k\sin\theta\cos\varphi+m\Omega_x)\right]\times\mathrm{sinc}\left[\frac{D_y}{2}(k\sin\theta\sin\varphi+n\Omega_y)\right] \quad (8)$$

Each mode function describes a beam in the space with its peak at the direction of $(\theta_{mn},\varphi_{mn})$ and $(\pi-\theta_{mn},\varphi_{mn})$, both satisfying the following:

$$\begin{cases} k\sin\theta_{mn}\cos\varphi_{mn}+m\Omega_x=0 \\ k\sin\theta_{mn}\sin\varphi_{mn}+n\Omega_y=0 \end{cases} \quad (9)$$

The wavevector of the mn-th mode at its peak direction $(\theta_{mn},\varphi_{mn})$ is denoted as $(k_{xmn},k_{ymn},k_{zmn})$, and

$$\begin{cases} k_{xmn}=k\sin\theta_{mn}\cos\varphi_{mn} \\ k_{ymn}=k\sin\theta_{mn}\sin\varphi_{mn} \\ k_{zmn}=k\cos\theta_{mn} \end{cases} \quad (10)$$

For a single-current sheet, it has been proposed in [28] that the mn-th mode is a propagation mode if k_{zmn} is real; otherwise, it is an evanescent mode. The main lobes of the propagation modes fall in the visible region of the antenna, while only part of the side lobes of the evanescent modes fall in the visible region. The far fields are mainly determined by those modes in the propagation constellation $\mathbb{P}$, where $\mathbb{P}$ is defined as the following [28]:

$$\mathbb{P}=\left\{(m,n)\in\mathbb{Z}^2:(m/N_x)^2+(n/N_y)^2\le1\right\} \quad (11)$$

Although part of the sidelobes of an evanescent mode may fall into the visible region and contribute to the far fields, its effect is trivial unless the amplitude of this evanescent mode is much larger than that of the propagation modes.

We can check from (7) to (9) that the constellations of the two current sheets are exactly the same as that of the single-current sheet that is centered at the origin, as defined in (11). The displacement in the z-axis only causes a phase-shift in all the propagation modes, which is $\exp(jk_zd)$ for the upper sheet, and $\exp(-jk_zd)$ for the lower one. The far field of each current sheet is mainly determined by the propagation modes associated with that current sheet. The total far fields of the two current sheets are the sum of the contributions

from the two sets of propagation modes, weighted by the phase shift corresponding to the center position in the z-axis, which can be expressed by the following:

$$F_{2a}(\theta,\varphi)=\sum_{m=-N_x}^{N_x}\sum_{n=-N_y}^{N_y}\left(I_{1mn}e^{jk_zd}+I_{2mn}e^{-jk_zd}\right)f_{mn}(\theta,\varphi) \tag{12}$$

with $(m,n)\in\mathbb{P}$.

Note that $f_{mn}(\theta_{mn},\varphi_{mn})=1$ and $f_{mn}(\theta_{pq},\varphi_{pq})=0$ if $p\neq m$ or $q\neq n$. Similar to handling a single-layer current, the property of the sinc functions enables us to solve the coefficients of the currents directly with the following equation:

$$I_{1mn}e^{jk_{zmn}d}+I_{2mn}e^{-jk_{zmn}d}=F_{2a}(\theta_{mn},\varphi_{mn}) \tag{13}$$

The far fields at the peak directions of the propagation modes in both the upper half space and the lower half space have to be used to solve the current coefficients. Making use of (9) and (10) we have the following:

$$\begin{cases} k_{xmn}=k\sin\theta_{mn}\cos\varphi_{mn}=-m\Omega_x=-km/N_x \\ k_{ymn}=k\sin\theta_{mn}\sin\varphi_{mn}=-n\Omega_y=-kn/N_y \end{cases} \tag{14}$$

From which k_{xmn}, k_{ymn}, θ_{mn}, and φ_{mn} can be determined. It is important to note the following:

$$k_{zmn}=\begin{cases} k\sqrt{1-(m/N_x)^2-(m/N_y)^2},\ \theta_{mn}\le\pi/2 \\ -k\sqrt{1-(m/N_x)^2-(m/N_y)^2},\ \theta_{mn}>\pi/2 \end{cases} \tag{15}$$

Therefore, we can derive the following:

$$\begin{cases} I_{1mn}=-A_{mn}\left[e^{j2|k_{zmn}|d}F_{2a}(\theta_{mn},\varphi_{mn})-F_{2a}(\pi-\theta_{mn},\varphi_{mn})\right] \\ I_{2mn}=A_{mn}\left[F_{2a}(\theta_{mn},\varphi_{mn})-e^{j2|k_{zmn}|d}F_{2a}(\pi-\theta_{mn},\varphi_{mn})\right] \end{cases} \tag{16}$$

where the coefficient is the following:

$$A_{mn}=\frac{je^{-j|k_{zmn}|d}}{2\sin(2|k_{zmn}|d)} \tag{17}$$

The realized far-field pattern can be evaluated with (12) and the two current distributions can be calculated with the following:

$$\begin{cases} I_1(x,y)=\sum_m\sum_n I_{1mn}e^{j(m\Omega_x x+n\Omega_y y)} \\ I_2(x,y)=\sum_m\sum_n I_{2mn}e^{j(m\Omega_x x+n\Omega_y y)} \end{cases} \tag{18}$$

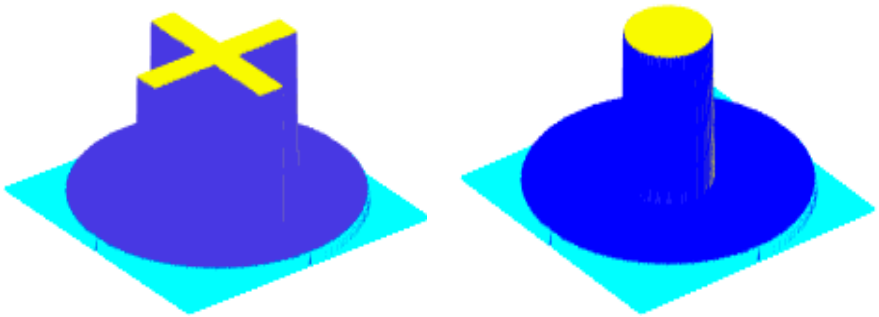
where I_{1mn} and I_{2mn} are given in (16) and $(m,n)\in\mathbb{P}$.

3. Synthesis Examples

In the first example, we are to realize a non-mirror-symmetrical far-field pattern with a cross-shaped footprint in the upper half space and a disk-shaped footprint in the lower half space. It is understood that in practical designs we have to define the footprint from specified radiation patterns. In our examples, we just skip this step and assign the footprint directly in the normalized k_x-k_y plane for the sake of convenience. The size of each bar of the cross-shaped beam is assumed to be 0.2×1.2, and the radius of the disk-shaped beam is 0.3, as shown in Figure 3.

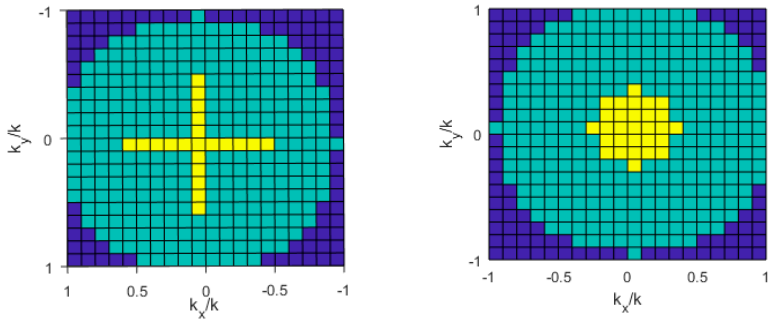
The structure of the two current sheets is still that shown in Figure 2. At first, we use a smaller source area of $D_x = D_y = 10\lambda$. The distance between the two sheets is chosen to be $\lambda/4$. The footprint in the normalized $k_x - k_y$ plane is shown in Figure 4, where the yellow area is the footprint and the cyan area is the propagation mode area with $(m, n) \in \mathbb{P}$. The peak direction of each mode is as follows:

$$\hat{\mathbf{k}}_{mn}(\theta_{mn}, \varphi_{mn}) = \left[\frac{k_{xmn}}{k}, \frac{k_{ymn}}{k}, \frac{k_{zmn}}{k}\right] = (\sin\theta_{mn}\cos\varphi_{mn}, \sin\theta_{mn}\sin\varphi_{mn}, \cos\theta_{mn})$$



(**a**) (**b**)

Figure 3. The prototype of the radiation pattern. (**a**) Upper half space. (**b**) Lower half space.



(**a**) (**b**)

Figure 4. The radiation footprint in the normalized $k_x - k_y$ plane for Example 1. (**a**) Upper half space. (**b**) Lower half space.

In the normalized $k_x - k_y$ plane, each peak direction corresponds to the center of a square. In this case, we can count from (11) that there are totally 317 propagation modes. With the beam structure in Figure 3, we can check that 21 of the propagation modes are used for forming the cross-shaped footprint, and 29 of them help to form the disk-shaped footprint.

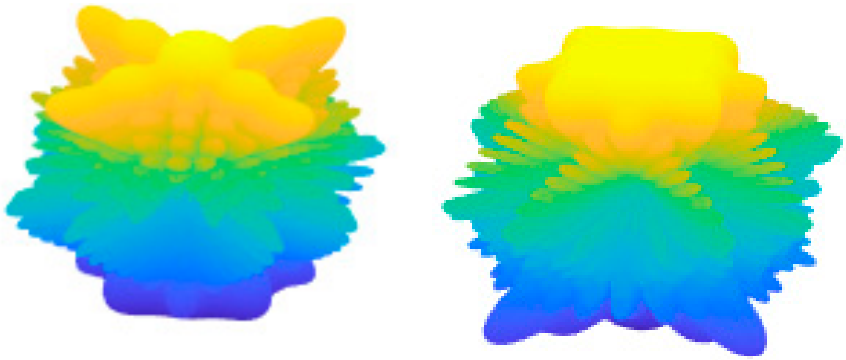
For the sake of brevity, we assume that the far field is one in the yellow area and zero in the cyan area. That is,

$$F_{2a}(\theta_m, \varphi_n) = \begin{cases} 1.0, \text{ in yellow region} \\ 0, \text{ in cyan region} \end{cases}$$

The realized radiation pattern is shown in Figure 5. Both the normal perspective view and the upside-down view are plotted to give a clearer illustration. Because the far-field pattern is assumed to change sharply in the edges of the footprint, and the sizes of the current sheets are relatively small, the sidelobe levels are relatively high. However, the cross-shaped and disk-shaped footprints are clearly demonstrated.

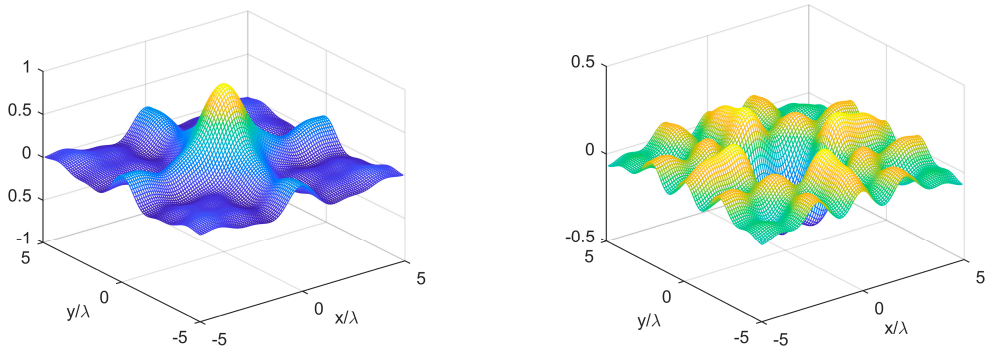
Since we have assumed the real-valued far field in the synthesis, we can check from (16) that $I_{1mn} = I^*_{2mn}$, hence the resultant currents on the two sheets are conjugated to each

other. We only give the normalized current distribution in the upper sheet in Figure 6. The current distribution on the middle line in the x-direction is shown in Figure 7.



(**a**) (**b**)

Figure 5. Realized pattern with current sheets of $10\lambda \times 10\lambda$. (**a**) Normal perspective view. (**b**) Upside down view.



(**a**) (**b**)

Figure 6. The current on the upper sheet. (**a**) Real part. (**b**) Imaginary part.

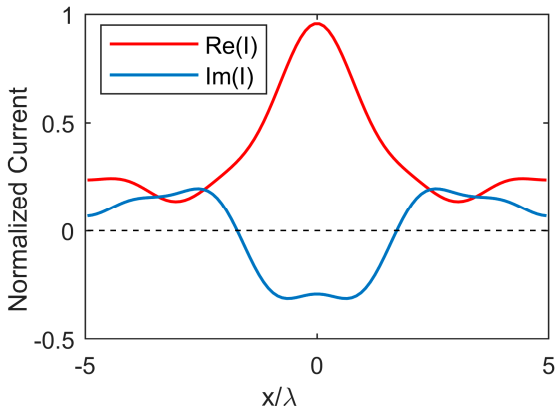
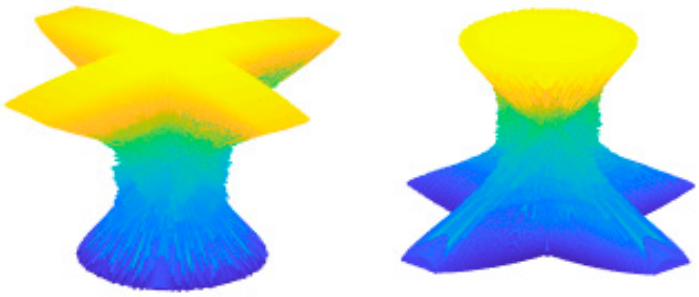


Figure 7. The current on the middle line of the upper sheet of Figure 6 in the x-direction.

In order to reduce the level of the sidelobes and realize a radiation pattern that is closer to the prototype, we re-synthesize it with a much larger source area of $D_x = D_y = 100\lambda$. The distance between the two sheets is still $\lambda/4$. Larger current sheets generate more propagation modes and provide a higher capability to shape the radiation pattern. In this case, it can be counted that there are a total of 31,417 propagation modes, 2821 of them are used for forming the cross-shaped footprint, and 4161 of them help to form the disk-shaped footprint, and both are much more than that in the first synthesis.

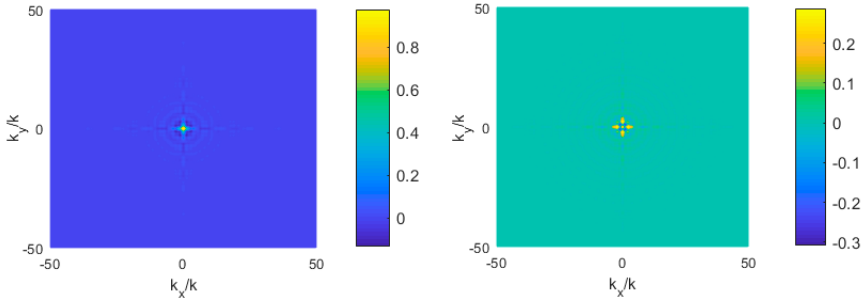
The realized radiation pattern is shown in Figure 8. As expected, the footprints are much clearer and the sidelobe levels are much lower when large current sheets are used.



(**a**) (**b**)

Figure 8. Realized pattern with current sheets of $100\lambda \times 100\lambda$. (**a**) Normal perspective view. (**b**) Upside down view.

The normalized current in the upper sheet is shown in Figure 9, and the current distribution on the middle line in the x-direction is shown in Figure 10. It can be seen that in most areas of the sheet the current is very small, which makes further thinning possible.



(**a**) (**b**)

Figure 9. Current distribution on one sheet. (**a**) Real part. (**b**) Imaginary part.

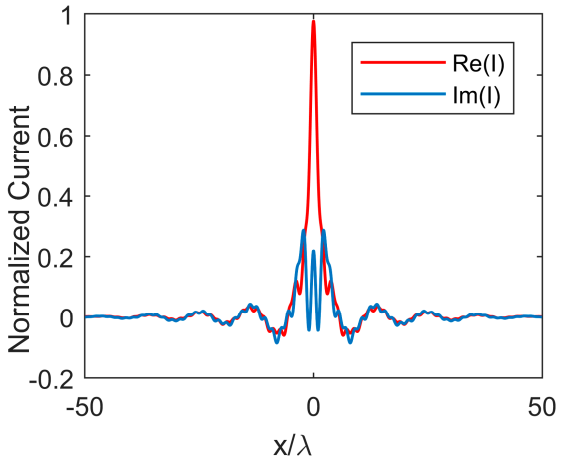


Figure 10. The current on the middle line of the upper sheet of Figure 9 in the x-direction.

The second example is to demonstrate that we can realize complex radiation patterns and meanwhile control their polarizations. The specified radiation footprint is shown in Figure 11. It is a circularly polarized (CP) square beam in the upper half space. The edge length is 0.125 in the normalized $k_x - k_y$ plane. The pattern in the lower half space consists of two linearly polarized (LP) beams forming the shapes of "S" and "J", as shown

in Figure 11b. For the CP beam, we assume that the $\hat{\theta}_x$ component of the far field is 1.0 and the $\hat{\theta}_y$ component of the far field is $j1.0$. For the LP beams, their far fields only have the $\hat{\theta}_x$ component with a value of 1.0. Furthermore, we have scaled by 0.5 all the amplitudes of those values at the edges of the beams and avoided sharp transitions in the radiation pattern, as can be seen in Figure 11.

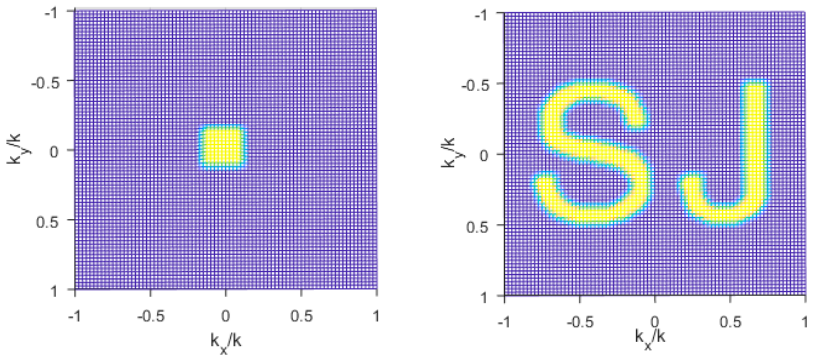


Figure 11. The radiation footprint in the normalized $k_x - k_y$ plane for Example 2. (**a**) Upper half space. (**b**) Lower half space.

We synthesize it with a source area of $D_x = D_y = 40\lambda$. The distance between the two sheets is $\lambda/4$. It can be counted that there are a total of 5025 propagation modes, and 169 of them are used for forming the square-shaped footprint and 1346 of them help to form the SJ-shaped footprint.

The realized radiation pattern is shown in Figure 12. Note that the square beam is circularly polarized, and the SJ-beams are linearly polarized. The axial ratios (ARs) at different ϕ planes are plotted in Figure 13, which clearly demonstrate that the ARs near $\theta = 0$, corresponding to the square beam, are very small (less than 1 dB).

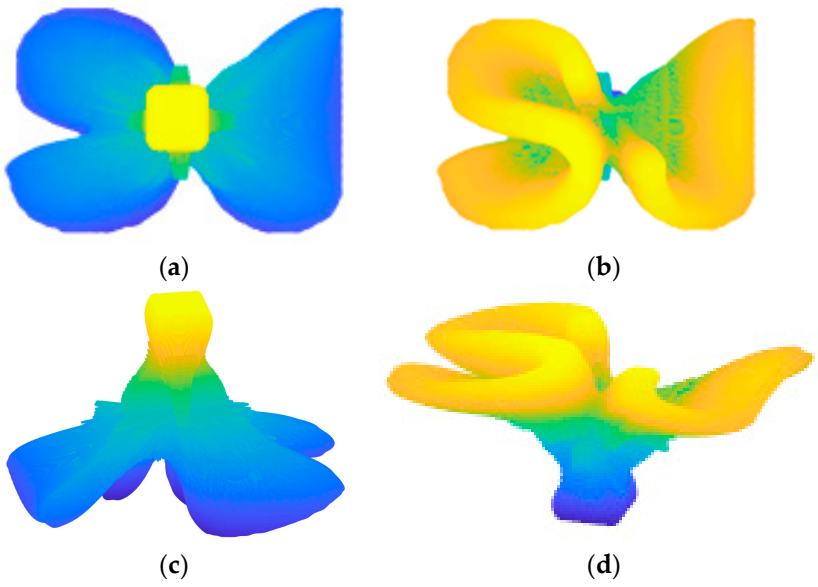


Figure 12. Realized pattern of Example 2. (**a**) Top view. (**b**) Bottom view. (**c**) Normal perspective view. (**d**) Upside-down perspective view.

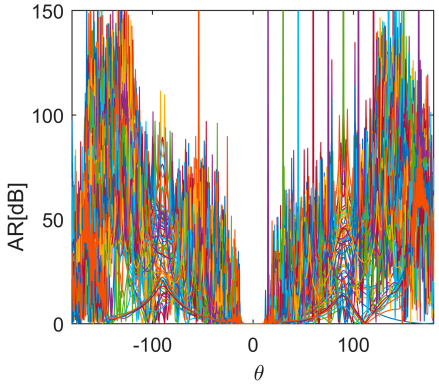


Figure 13. AR (θ) of the far fields at different ϕ planes.

The synthesized current distribution on one sheet is plotted in Figure 14. Its $x-$ component is much more complicated because it contributes to all beams in the two sides, while its $y-$component mainly contributes to the CP beam.

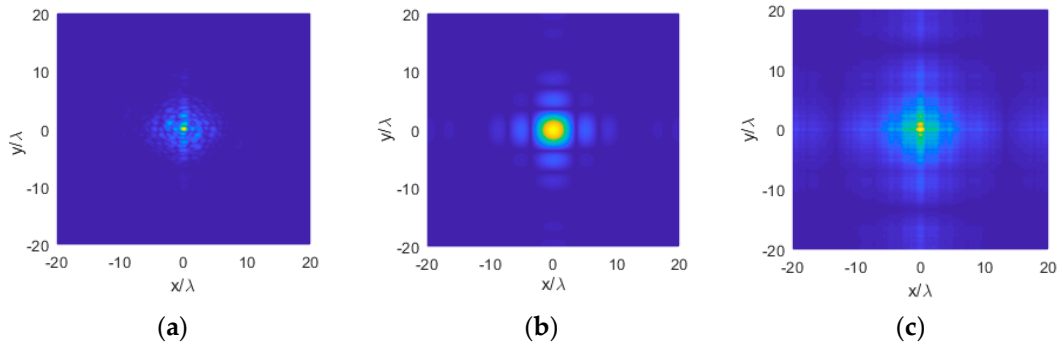


Figure 14. Current distributions. (**a**) $x-$component. (**b**) $y-$component. (**c**) Total amplitude.

4. Discussions and Conclusions

An important issue is the effect of the distance between the two current sheets. It can be seen from (7) that, although the interpolation of the pattern is mainly determined using the sinc mode functions, the phase shift term $\exp(jk_z d)$ is also a function with respect to θ, since $k_z = k\cos\theta$. This will affect the interpolation behavior. A simple strategy is to choose a small d so that $\exp(jk_z d)$ is a slow-varying function compared to the sinc functions. To further exploit this issue, we consider a broad-side antenna array in which $k_{zmn} \approx k$ in the main beam. According to (16) and (17), the currents required to realize the prescribed pattern are minimum if we choose $\sin 2kd = 1$, or equivalently, the distance between the two current sheets is $2d = \lambda/4$. It can be readily checked that the phase shift caused by the term $\exp(jkd\cos\theta)$ is smaller than $\pi/4$ for all propagation modes. The side effect to the interpolation is negligible, as has been demonstrated with the examples.

In the proposed method, only propagation harmonic components of the currents are taken into account for synthesizing a required radiation pattern. In practical situation, it is difficult for us to suppress all harmonic components of currents corresponding to the evanescent modes. However, with some kinds of filtering technique, it is possible to exclude those current components that generate evanescent modes with large sidelobes falling in the visible region.

With the proposed direct synthesis method, non-mirror-symmetrical array patterns can be effectively synthesized using two parallel current sheets, in which it is assumed that the distributions of the two currents are not affected by each other. Although this assumption may be different from the practical situations, the direct synthesis process is perhaps helpful to give a reference for practical designs, as the synthesis process is quite

simple and easy to implement. If the realized pattern is not satisfactory, we can simply adjust the prototype of the radiation pattern and repeat the synthesis process once again.

To summarize, we have shown that it is possible to realize the radiation patterns in the two half spaces separately with two parallel continuous current sheets. However, in practical applications, it may be difficult to realize a continuous current distribution. We may need to spatially sample the continuous current and realize the far-field pattern using discrete elements with a half-wavelength spacing. This discretization corresponds to the spatial sampling frequency of $2\pi/(0.5\lambda) = 2k$ in k-space, which is two times higher than the largest spatial frequency k of the propagation modes. Therefore, if the current is band-limited expressed by (18), and the continuous current is sampled with spacing of smaller than or equal to half wavelength, the resultant higher harmonic components in the current brings only evanescent modes, and only a small part of their side lobes will affect the far-field pattern.

In our future work, we will investigate the effect of different sampling strategies together with the proper feeding techniques for the resultant discrete array.

Author Contributions: Conceptualization, methodology, original draft, funding acquisition, calculation, G.X.; Verification, review and editing, T.Z. and R.L. All authors have read and agreed to the published version of the manuscript.

Funding: This research was funded by the National Key R&D Program of China, China (Grant No. 2019YFB2204703), the National Natural Science Foundation of China, China (Grant No. 61831016), the National Natural Science Foundation of China, China (Grant 62188102).

Data Availability Statement: Not applicable.

Conflicts of Interest: The authors declare that the research was conducted in the absence of any commercial or financial relationships that could be construed as a potential conflict of interest.

References

1. Ares, F.; Elliott, R.S.; Moreno, E. Design of planar arrays to obtain efficient footprint patterns with an arbitrary footprint boundary. *IEEE Trans. Antennas Propag.* **1994**, *42*, 1509–1514. [CrossRef]
2. Bucci, O.M.; D'Elia, G.; Mazzarella, G.; Panariello, G. Antenna pattern synthesis: A new general approach. *Proc. IEEE* **1994**, *82*, 358–371. [CrossRef]
3. Rodriguez, J.A.; Ares, F.; Lopez, P.; Moreno, E. Quasi-analytical synthesis of moderate and large arrays radiating arbitrary 'Star-Shaped' footprint patterns [Antenna Designer's Notebook]. *IEEE Antennas Propag. Mag.* **2007**, *49*, 105–112.
4. Ares, F.; Fondevila-Gomez, J.; Franceschetti, G.; Moreno-Piquero, E.; Rodriguez-Gonzalez, J.A. Synthesis of very large planar arrays for prescribed footprint illumination. *IEEE Trans. Antennas Propag.* **2008**, *56*, 584–589. [CrossRef]
5. Aghasi, A.; Amindavar, H.; Miller, E.L.; Rashed-Mohassel, J. Flattop footprint pattern synthesis through the design of arbitrary planar-shaped apertures. *IEEE Trans. Antennas Propag.* **2010**, *58*, 2539–2552. [CrossRef]
6. Keizer, W.P.M.N. Fast low-sidelobe synthesis for large planar array antennas utilizing successive fast Fourier transforms of the array factor. *IEEE Trans. Antennas Propag.* **2007**, *55*, 715–722. [CrossRef]
7. Caorsi, S.; Lommi, A.; Massa, A.; Pastorino, M. Peak sidelobe reduction with a hybrid approach based on GAs and different sets. *IEEE Trans. Antennas Propag.* **2004**, *52*, 1116–1121. [CrossRef]
8. Yang, K.; Zhao, Z.; Liu, Q.H. Fast pencil beam pattern synthesis of large unequally spaced antenna arrays. *IEEE Trans. Antennas Propag.* **2013**, *61*, 627–634. [CrossRef]
9. Haupt, R.L. Thinned arrays using genetic algorithms. *IEEE Trans. Antennas Propag.* **1994**, *42*, 993–999. [CrossRef]
10. Johnson, J.M.; Rahmat-Samii, V. Genetic algorithms in engineering electromagnetics. *IEEE Antennas Propag. Mag.* **1997**, *39*, 7–21. [CrossRef]
11. Boeringer, D.; Werner, D. Particle swarm optimization versus genetic algorithms for phased array synthesis. *IEEE Trans. Antennas Propag.* **2004**, *52*, 771–779. [CrossRef]
12. Meijer, C.A. Simulated annealing in the design of thinned arrays having low sidelobe levels. In Proceedings of the 1998 South African Symposium on Communications and Signal Processing-COMSIG'98 (Cat. No. 98EX214), Rondebosch, South Africa, 8 September 1998.
13. Fuchs, B. Synthesis of sparse arrays with focused or shaped beam pattern via sequential convex optimizations. *IEEE Trans. Antennas Propag.* **2012**, *60*, 3499–3503. [CrossRef]
14. Prisco, G.; D'Urso, M. Maximally sparse arrays via sequential convex optimizations. *IEEE Antennas Wireless Propag. Lett.* **2012**, *11*, 192–195. [CrossRef]

15. Quevedo-Teruel, O.; Rajo-Iglesias, E. Ant colony optimization in thinned array synthesis with minimum sidelobe level. *IEEE Antennas Wireless Propag. Lett.* **2006**, *5*, 349–352. [CrossRef]
16. Chellapilla, K.; Hoorfar, A. Evolutionary programming: An efficient alternative to genetic algorithms for electromagnetic optimization problems. In Proceedings of the IEEE Antennas and Propagation Society International Symposium. 1998 Digest. Antennas: Gateways to the Global Network, Atlanta, GA, USA, 21–26 June 1998.
17. Haupt, R.L. Interleaved thinned linear arrays. *IEEE Trans. Antennas Propag.* **2005**, *53*, 2858–2864. [CrossRef]
18. Leeper, D. Isophoric arrays-massively thinned phased arrays with well controlled sidelobes. *IEEE Trans. Antennas Propag.* **1999**, *47*, 1825–1835. [CrossRef]
19. Oliveri, G.; Donelli, M.; Massa, A. Linear array thinning exploiting almost difference sets. *IEEE Trans. Antennas Propag.* **2009**, *57*, 3800–3812. [CrossRef]
20. Anselmi, N.; Gottardi, G.; Oliveri, G.; Massa, A. A total-variation sparseness-promoting method for the synthesis of contiguously clustered linear arrays. *IEEE Trans. Antennas Propag.* **2019**, *67*, 4589–4601. [CrossRef]
21. Aldhafeeri, A.; Rahmat-Samii, Y. Brain storm optimization for electromagnetic applications: Continuous and discrete. *IEEE Trans. Antennas Propag.* **2019**, *67*, 2710–2722. [CrossRef]
22. Bucci, O.M.; D'Urso, M.; Isernia, T.; Angeletti, P.; Toso, G. Deterministic synthesis uniform amplitude sparse arrays via new density taper techniques. *IEEE Trans. Antennas Propag.* **2010**, *58*, 1949–1958. [CrossRef]
23. Kumar, B.P.; Branner, G.R. Generalized analytical technique for the synthesis of unequally spaced arrays with linear, planar, cylindrical or spherical geometry. *IEEE Trans. Antennas Propag.* **2005**, *53*, 621–633. [CrossRef]
24. Woodward, P.M. A method for calculating the field over a plane aperture required to produce a given polar diagram. *J. IEEE* **1946**, *93*, 1554–1558. [CrossRef]
25. Miller, E.K.; Lager, D.L. Radiation field analysis and synthesis using Prony's method. *Electron. Lett.* **1978**, *14*, 180–182. [CrossRef]
26. Miller, E.K. Using Prony's method to synthesize discrete arrays for prescribed source distributions and exponentiated patterns. *IEEE Antennas Propag. Mag.* **2015**, *57*, 147–163. [CrossRef]
27. Balanis, C.A. *Antenna Theory Analysis and Design*, 3rd ed.; John Wiley & Sons, Inc.: Hoboken, NJ, USA, 2005; Chapter 7.
28. Xiao, G.B.; Liu, R. Direct method for reconstructing the radiating part of a planar source form its far-fields. *Electronics* **2022**, *11*, 3852. [CrossRef]
29. Pizzo, A.; Marzetta, T.L.; Sanguinetti, L. Degrees of freedom of holographic MIMO channels. In Proceedings of the 2020 IEEE 21st International Workshop on Signal Processing Advances in Wireless Communications (SPAWC), Atlanta, GA, USA, 26–29 May 2020; pp. 1–5.

Disclaimer/Publisher's Note: The statements, opinions and data contained in all publications are solely those of the individual author(s) and contributor(s) and not of MDPI and/or the editor(s). MDPI and/or the editor(s) disclaim responsibility for any injury to people or property resulting from any ideas, methods, instructions or products referred to in the content.